Journal of Materials Chemistry A

ROYAL SOCIETY OF CHEMISTRY

PAPER

View Article Online
View Journal | View Issue

Cite this: J. Mater. Chem. A, 2026, 14, 9480

Irreversible phase transitions in $BiFeO_3$–$SrTiO_3$ lead-free piezoceramics

Songhao Fu, [a] Muhammad Wasim,[b] Hareem Zubairi,[c] Xiaojiao Liu,[d] Annette K. Kleppe,[d] Xinzhen Wang, [e] Antonio Feteira, [b] Ge Wang *[c] and Zhilun Lu *[a]

Received 16th September 2025
Accepted 14th January 2026

DOI: 10.1039/d5ta07591b

rsc.li/materials-a

The development of high-performance lead-free piezoelectric materials has gained significant attention due to environmental concerns regarding lead toxicity. In this study, through *in situ* poling synchrotron X-ray diffraction (XRD), dielectric spectroscopy, and ferroelectric measurements, we demonstrate an irreversible transition from non-ergodic relaxor behaviour to long-range ferroelectric ordering under applied electric fields in $(1-x)BiFeO_3$-$xSrTiO_3$ with MnO_2 addition (BF-ST-Mn). The optimal composition with $x = 0.44$ exhibits an electrostrain of ~0.10% at 80 kV cm^{-1} through an irreversible pseudo-cubic to rhombohedral structural transformation followed by ferroelectric domain switching. This stands in sharp contrast to BF-ST-Nb systems, where strong random fields preserve a stable ergodic relaxor state; instead, the BF-ST-Mn system overcomes moderate pinning to establish irreversible long-range rhombohedral order. Synchrotron XRD reveals an initial structural transformation during the first electrical cycle, followed by domain switching in subsequent cycles. It provides promising pathways for lead-free actuator applications requiring high electrostrain at moderate driving fields.

1. Introduction

Ferroelectric materials are extensively used in many applications such as piezoelectric actuators[1] and dielectric capacitors.[2–5] Traditional piezoelectric ceramics, particularly $Pb(Zr_xTi_{1-x})O_3$ (PZT), have dominated commercial applications due to their excellent performance.[6,7] However, mounting environmental concerns regarding lead toxicity have created an urgent need for sustainable alternatives. Recent developments in lead-free piezoelectric materials have yielded remarkable advances,[8–11] with several emerging material systems now achieving performance metrics that rival conventional PZT ceramics. The most lead-free piezoelectric materials are potassium sodium niobate (KNN)-based,[12] sodium bismuth titanate (NBT)-based,[13,14] and bismuth ferrite (BF)-based[15] systems. Each has its own advantages and disadvantages.

KNN-based materials exhibit impressive piezoelectric coefficients (d_{33}) among lead-free alternatives but face challenges including atmospheric sensitivity, temperature instability, and poor reproducibility due to chemical inhomogeneity,[16] though recent advances using $KNaCO_3$ precursors have improved chemical homogeneity and lowered phase transition temperatures.[17] While NBT-based materials demonstrate superior electrostrain performance (0.7%),[18,19] they are constrained by low depolarisation temperatures (<150 °C)[20] that limit the operational temperature ranges.

Pure $BiFeO_3$ (BF) is a typical multiferroic material that combines a high Curie temperature (~830 °C)[21] with visible-light catalytic activity.[22] However, its high leakage current caused by the presence of oxygen vacancies and mixed Fe^{2+}/Fe^{3+}/Fe^{4+} valence states[23] severely limits practical applications, whilst maintaining single-phase synthesis and addressing high conductivity issues remain primary challenges. To overcome these limitations, the $BiFeO_3$–$BaTiO_3$ (BF–BT) solid solution has emerged as the most extensively researched BF-based system.[24,25] BF–BT demonstrates well-defined phase relationships with morphotropic phase boundaries at 30–35 mol% BT composition, where the coexistence of rhombohedral and pseudo-cubic phases optimises the piezoelectric response, exhibiting a significant piezoelectric response (d_{33} ~ 134–180 pC N^{-1}).[26,27] The core advantage of BF–BT lies in its exceptional high-temperature performance, with a Curie temperature significantly superior to that of PZT.[28,29] Despite the challenge of bismuth volatilisation during sintering, BF–BT represents one of the most promising candidates for high-temperature

[a]School of Chemical and Process Engineering, University of Leeds, Leeds, LS2 9JT, UK. E-mail: z.lu@leeds.ac.uk

[b]School of Engineering and Built Environment, Sheffield Hallam University, Sheffield, S1 1WB, UK

[c]Department of Materials, University of Manchester, Manchester, M13 9PL, UK. E-mail: ge.wang@manchester.ac.uk

[d]Diamond Light Source Ltd, Harwell Science and Innovation Campus, Didcot, OX11 0DE, UK

[e]School of Materials Science and Engineering, Shandong University of Science and Technology, Qingdao, 266590, China

piezoelectric applications, demonstrating exceptional thermal stability above 400 °C.[30,31]

The optimisation mechanisms for converse piezoelectric properties, including electrostrain, in piezoelectric materials primarily include domain switching,[32] structural transformations,[33] and lattice strain.[34] For example, Pramanick *et al.* studied the response of undoped and La/Fe-doped PZT ceramics under subcoercive fields and revealed that non-180° domain wall motion with Rayleigh-type behaviour is the predominant mechanism responsible for the Rayleigh characteristics of the d_{33} piezoelectric coefficient.[35] In contrast, NBT-based materials exhibit unique reversible and irreversible structural transformations. Liu *et al.*[36] found that non-stoichiometric $0.99Bi_{0.505}(Na_{0.8}K_{0.2})_{0.5-x}TiO_3$-$0.01SrTiO_3$ (BNKST) ceramics at the critical composition $x = 0.015$ exhibit excellent strain characteristics (the positive strain $S_{pos} = 0.42\%$, $d^*_{33} = 479$ pm V^{-1}), primarily attributed to reversible relaxor–ferroelectric phase transitions. Additionally, the occurrence of an electric field-induced irreversible structural transformation has been reported for $(1-x)$NBT-xNaNbO$_3$ ($x = 0.02$ and 0.04).[37]

BF–BT based materials typically optimise strain through reversible structural transformations or multiple nanoscale symmetries with a common polarisation axis. Chen *et al.* employed *in situ* synchrotron powder XRD analysis to demonstrate that 0.64BF-0.36BT bulk ceramics achieve 0.38% electrostrain through a nearly reversible phase transition from a pseudo-cubic to a rhombohedral phase under a high electric field.[38] The large electric-field-induced strain in these ceramics originates from a combination of lattice distortion, non-180° domain switching, and phase transitions.

While ferroelectric and piezoelectric data remain limited compared to BF–BT systems, with few systematic studies on BF–ST, research reveals both promising properties and significant challenges. Wang *et al.*[39] prepared $(1-x)$BF-xST ceramics with 0.15 wt% MnO_2 across compositions from 0.32 to 0.44 near the morphotropic phase boundary (MPB), where the optimal composition at $x = 0.38$ exhibited the largest grain size of 5.66 μm with a unique core–shell structure, demonstrating a high P_r of 51.2 μC cm^{-2} and d_{33} of 72 pC N^{-1}. The 75ST-25BF-3Nb ceramics prepared by Wang *et al.*[40] exhibit excellent dielectric properties: low loss ($\tan\delta \approx 0.1$) and a stable dielectric constant ($\varepsilon_r \approx 700$ @ 1 kHz). Impedance spectroscopy indicates that Nb doping significantly enhances both resistivity and activation energy, forming a conductive core–insulating shell structure. Our previous study[41] revealed the maximum electrical strain (0.15%) and existence of multiple symmetric nano-polar regions in 60BF-40ST-1Nb ceramics, supporting the view on the origin of electrostrain in BF–BT-based ceramics.[42] This view holds that the observed electrostrain is not caused by the field-induced relaxor-to-long-range ferroelectric transition; instead, it originates from the distortion of local polar regions along the applied field direction within multiple local symmetries, and these regions lack long-range correlations. These multiple nanoscale distorted symmetries at the local scale enhance the overall electrostrain performance. Rather than relying on domain switching or structural transformations, these materials maintain a pseudo-cubic average structure whilst achieving high electrostrain through distinct local structural configurations.

Nb_2O_5 has been added in previous studies to minimise electronic conductivity;[41] however, the E_c (80 kV cm^{-1}) of 60BF-40ST-1Nb ceramics is quite high compared to E_c values (~45 kV cm^{-1}) from other research[43] that may be due to Nb^{5+} donor doping. Despite Nb^{5+} typically acting as a donor dopant that softens ferroelectrics in PZT,[44] the unexpectedly high E_c suggests that other defect mechanisms or structural effects dominate in 60BF-40ST-1Nb ceramics. Additionally, based on our previous research,[41] the $(1-x)$BF-xST material undergoes a transition from ferroelectric to relaxor ferroelectric behaviour between $x = 0.4$ and $x = 0.5$.

Therefore, in this work, we added 0.2 wt% MnO_2 into $(1-x)$BF-xST ceramics at four compositions ($x = 0.42$, 0.44, 0.46, and 0.48) within the optimal performance range and systematically studied their dielectric, ferroelectric and piezoelectric properties. We expected that MnO_2 addition would only decrease the conductivity but not affect the intrinsic ferroelectric properties of BF–ST. *In situ* poling synchrotron XRD was employed to rationalise the origin of the electrostrain for $x = 0.44$.

2. Experimental section

Analytical-grade Bi_2O_3 (Sigma-Aldrich, 99.9%), Fe_2O_3 (Alfa Aesar, 99.945%), $SrCO_3$ (Sigma-Aldrich, 99.9%), TiO_2 (Sigma-Aldrich, 99.9%), and MnO_2 (Sigma-Aldrich, 99.0%) served as raw materials for synthesising $(1-x)$BF-xST ceramics ($x = 0.42$, 0.44, 0.46, and 0.48) with 0.2 wt% MnO_2 addition *via* a solid-state reaction. After weighing the stoichiometric amount of dry powder, it was ball-milled for 8 hours in isopropanol containing Y_2O_3-stabilized ZrO_2 grinding media. Subsequent processing involved drying and calcining the mixed powder at 800 °C for 2 hours, followed by adding 0.2 wt% MnO_2 and ball-milling for another 8 hours. Following uniaxial pressing, sintering was conducted at 1100–1150 °C for 2 hours with both heating and cooling rates of 5 °C min^{-1}.

Microstructural analysis was conducted using a Hitachi TM3030Plus scanning electron microscope equipped with backscattered electron (BSE) and energy-dispersive spectroscopy (EDS) capabilities for examining the original ceramic surfaces. Silver paste electrodes were applied to the samples, and temperature-dependent dielectric properties were subsequently measured using an Agilent 4184A precision LCR meter across a temperature range from room temperature to 550 °C. Testing frequencies of 1, 10, 100 kHz, and 1 MHz were employed, with geometric factor corrections (thickness/surface area) being applied to all dielectric data. Ferroelectric characterisation was performed using an aixACCT TF 2000E FE tester operated at 1 Hz to generate bipolar polarisation-electric field (P-E) and strain-electric field (S-E) hysteresis loops.

In situ poling synchrotron XRD was performed at Beamline I15, Diamond Light Source, as schematically shown in Fig. 1. The X-ray energy was 72 keV corresponding to a wavelength of 0.1722 Å. Ceramic pellet specimens were cut into rectangular bars with dimensions of 5 mm (length), 1 mm (width) and 0.4 mm (thickness). Ceramic bars were painted with silver

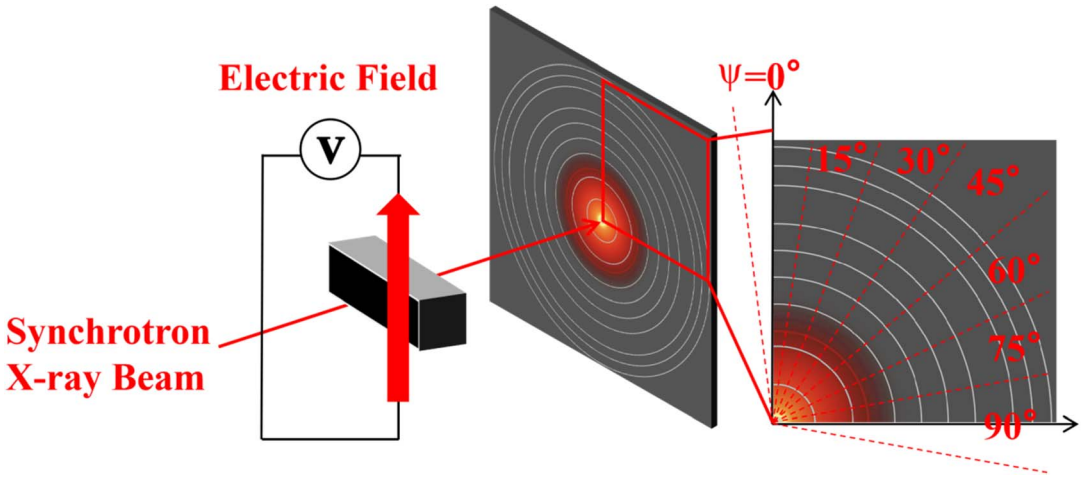

Fig. 1 Schematic of the *in situ* poling synchrotron XRD experimental setup.

electrodes on top and bottom sides, followed by firing at 600 °C for 2 hours. During the measurements, ceramic bar samples were placed in a custom polyimide holder within silicon oil. An AC electric field was applied to the sample using a high voltage amplifier (Matsusada EC-10).

The X-ray beam was focussed to 76 μm × 115 μm ($V \times H$). Data were collected in transmission geometry under electric fields up to 100 kV cm^{-1} with a step of 10 kV cm^{-1}. A Pilatus3 X CdTe 2M was used to capture the 2D diffraction data. The obtained diffraction rings were "caked" (reduced) into 1D diffraction patterns at every 15°. Here, $\psi = 0°$ and $\psi = 90°$ represent the direction parallel and perpendicular to the applied field, respectively. Peak positions and intensities were obtained using pseudo-Voigt functions by TOPAS 6.

3. Results and discussion

3.1 Crystal structure and microstructure

As shown in Fig. 2, the XRD Rietveld refinement analysis of $(1-x)$BiFeO$_3$-xSrTiO$_3$ (x = 0.42, 0.44, 0.46, 0.48) ceramics reveals that a single pseudo-cubic perovskite phase (space group $Pm\bar{3}m$) is formed by all components at room temperature, confirming that a stable solid solution is formed between BF and ST within this composition range. As shown in Table S1, with increasing ST content, the lattice contracts: the lattice constant a decreases from 3.94588(5) to 3.94287(4) Å ($\Delta a = -0.00301$ Å), and the unit cell volume contracts from 61.43723(2) to 61.29674(18) Å^3 ($\Delta V = -0.1405$ Å^3). This lattice contraction can be attributed to a smaller unit cell volume for ST relative to BF. Good refinement quality is achieved, with the goodness-of-fit factor (GOF) maintained within the ideal range of 1.26–1.39, indicating that the reliability of the single-phase structure is confirmed.

Fig. 3 illustrates the original surface morphology of $(1-x)$BF-xST ceramics at compositions of $x = 0.42$, 0.44, 0.46, and 0.48. All compositions display distinct grain boundaries; however, variations in grain size are evident within the same composition. Notably, samples with $x = 0.42$ and $x = 0.48$ (Fig. 3a and d) present a limited number of intergranular pores, whereas samples with $x = 0.44$ and $x = 0.46$ exhibit no apparent cracks or pores (Fig. 3b and c). Furthermore, the morphology of the $x = 0.44$ and $x = 0.46$ demonstrates higher density and surface smoothness, which is anticipated to enhance the dielectric breakdown strength by minimising electric field distortion.[45]

Grain size distribution analysis (Fig. 4) indicates that as the ST content (x) increases, the grain size does not follow a monotonic trend but remains consistently at the micron scale. The micrographs reveal a dense microstructure characterised by equiaxed grains and negligible porosity, corresponding to a relative density of approximately 95%. Among these, the smallest grain size is observed at $x = 0.48$, with an average of 1.68 μm (standard deviation: ±0.66 μm), while the largest grain size is noted at $x = 0.46$, averaging 3.90 μm (standard deviation: ±1.26 μm). Coarser grain sizes contribute to more uniform grain sizes in the samples with $x = 0.44$ and $x = 0.48$ (Fig. 4b and d). Based on the aforementioned analysis, the sample with $x = 0.42$ contains a limited number of pores and coarser grain sizes, while the sample with $x = 0.46$ exhibits a denser and flatter morphology but has excessively coarse grain sizes. Coarser grain sizes may increase the number of domain wall-grain boundary intersections, resulting in localised regions of concentrated electric fields and potentially heightening the risk of breakdown in the sample.[46] Conversely, the sample with $x = 0.48$ possesses the finest grain size but contains pores and displays an uneven surface. It is worth noting that the difference in grain size is mainly caused by subtle differences in the final sintering temperature. In order to obtain high-density ceramics, for every 0.02 increment in ST, the sintering temperature is raised by approximately 10–20 °C.

3.2 Dielectric properties

The temperature dependence of the dielectric properties of the $(1-x)$BF-xST series ceramics over a wide temperature range from 25 to 550 °C was investigated. Fig. 5 presents the temperature dependence of the dielectric constant (ε_r) and dielectric loss ($\tan\delta$) at four frequencies: 1 kHz, 10 kHz, 100 kHz, and 1 MHz. All samples exhibit distinct dielectric peaks in

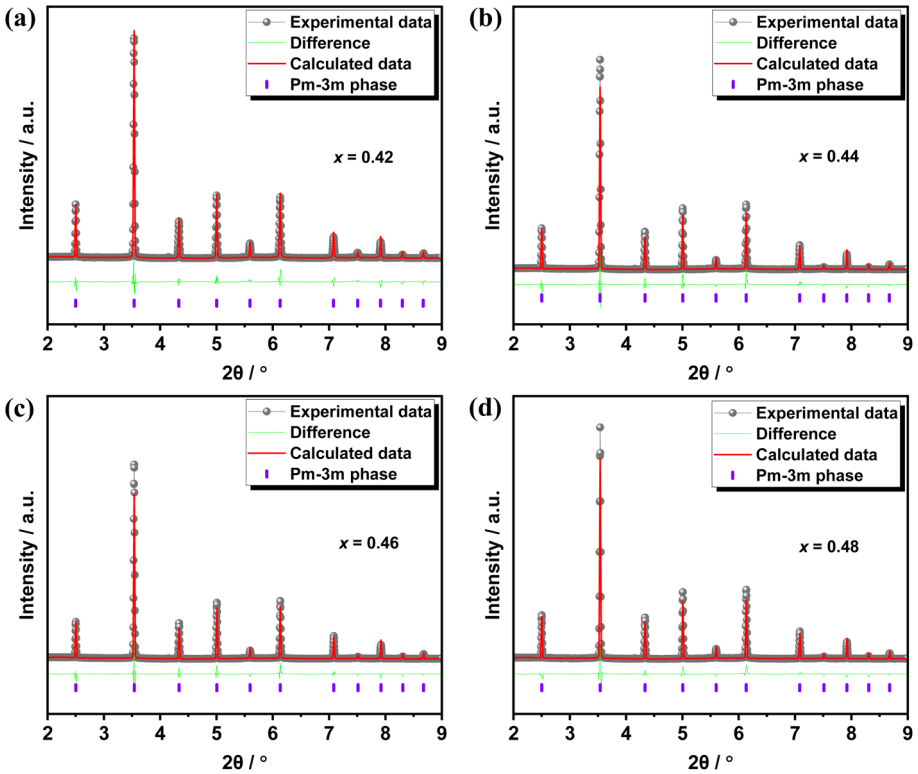

Fig. 2 Room temperature synchrotron XRD pattern and corresponding Rietveld refinement results for (1 − x)BF-xST ceramics, (a) x = 0.42, (b) x = 0.44, (c) x = 0.46, and (d) x = 0.48.

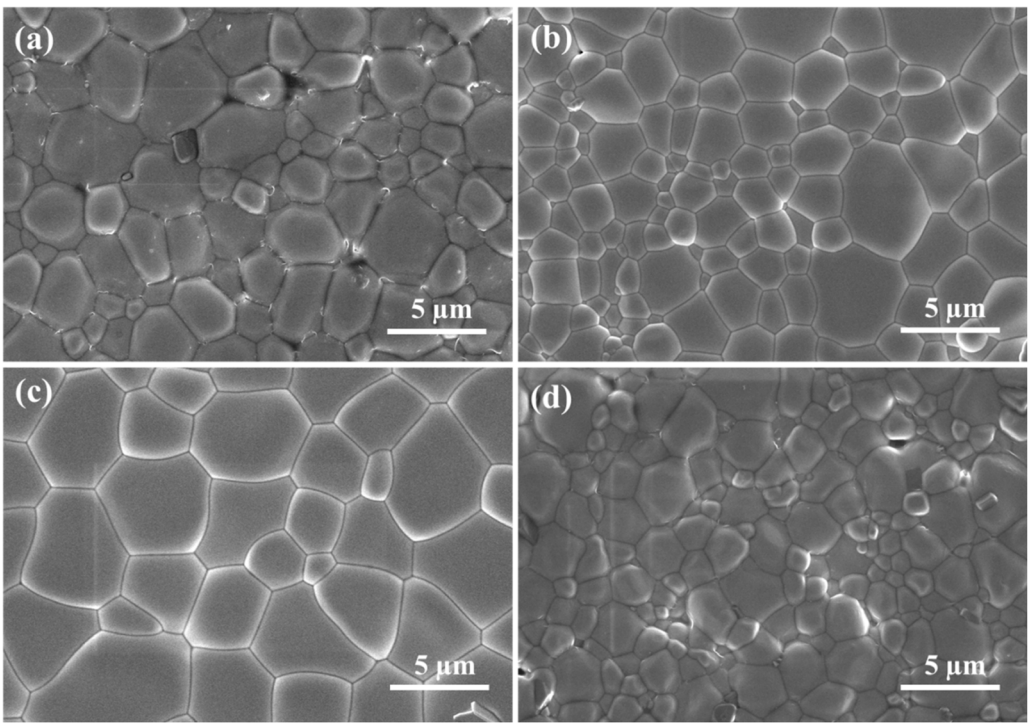

Fig. 3 Secondary Electron (SE) image of the original surface of (1 − x)BF-xST ceramics, (a) x = 0.42, (b) x = 0.44, (c) x = 0.46, and (d) x = 0.48.

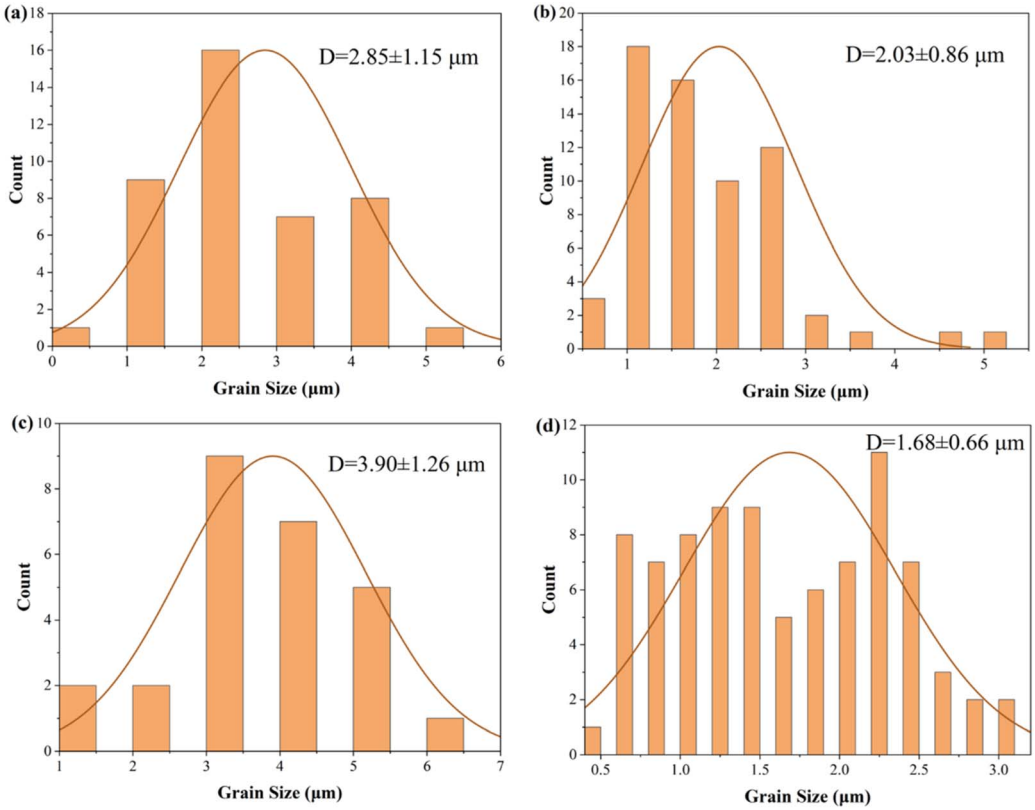

Fig. 4 Statistical diagram of (1 − *x*)BF-*x*ST ceramic particle size distribution, (a) $x = 0.42$, (b) $x = 0.44$, (c) $x = 0.46$, and (d) $x = 0.48$.

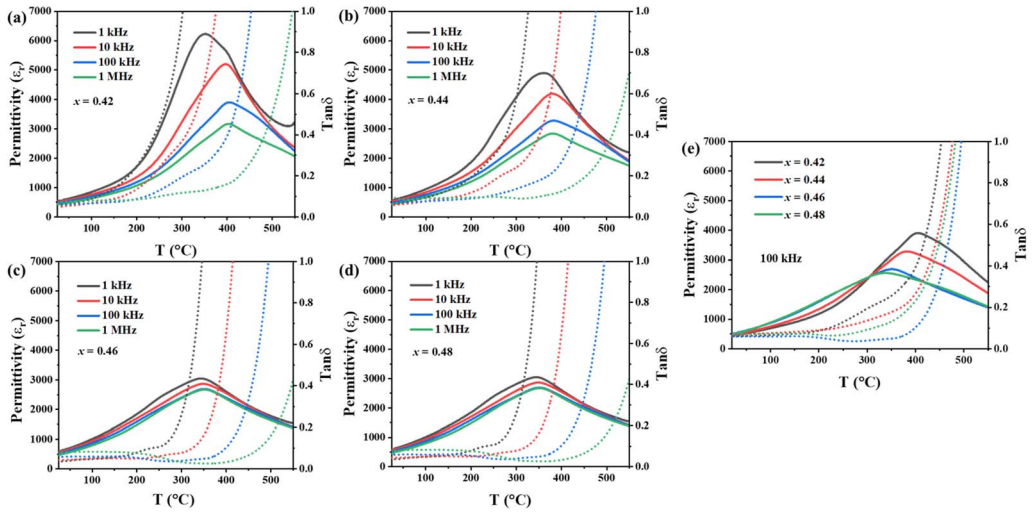

Fig. 5 (a) The temperature dependence of dielectric permittivity (ε_r *vs. T*) and loss (tan δ *vs. T*) of (1 − *x*)BF-*x*ST ceramics, (a) $x = 0.42$, (b) $x = 0.44$, (c) $x = 0.46$, (d) $x = 0.48$, and (e) The temperature dependence of ε_r and tan δ compared at 100 kHz.

their temperature spectra. As the ST content x increases, the dielectric peak broadens significantly, demonstrating a pronounced dispersion phenomenon. The maximum dielectric constant (ε_m) decreases markedly with increasing x, whereas dielectric loss (tan δ) generally decreases gradually with increasing x. Furthermore, the extent to which dielectric properties are influenced by changes in test frequency diminishes significantly with increasing x. These characteristics, including the decrease in ε_m, peak broadening, and reduced frequency dispersion effect indicate that as the ST content increases, the material's relaxation behaviour is enhanced.[47]

To facilitate a clearer comparison of the phase transition temperatures and dielectric loss among different compositions, Fig. 5e illustrates a comparison of ε_r and tan δ *versus*

temperature at a fixed frequency of 100 kHz for various compositions ($x = 0.42$, 0.44, 0.46, 0.48). The temperature (T_m) corresponding to the peak dielectric constant gradually shifts to lower temperatures as x increases. At the same temperature, the sample with $x = 0.46$ exhibits the lowest dielectric loss. The decrease in T_m with increasing ST content x may fundamentally stem from the introduction of ST significantly altering the crystal structure of the BF-based ceramic.[48] This structural change affects the stability of ferroelectric ordering, leading to a shift in the phase transition temperature toward lower temperatures and simultaneously inducing stronger relaxation characteristics, manifested as the aforementioned broadening, dispersion, and weakening of frequency dispersion of the dielectric peak. The T_m values of various BF-based ceramics are compared in Table 1.

3.3 Ferroelectric and piezoelectric properties

Fig. 6 illustrates the P-E and S-E loops of ceramic materials with compositions $(1 - x)$BF-xST ($x = 0.42$, 0.44, 0.46, 0.48) at room temperature under an electric field of 80 kV cm^{-1}. For compositions $x = 0.42$ and $x = 0.44$, both the P-E and S-E loops exhibit typical ferroelectric characteristics, marked by distinct saturation polarisation, significant residual polarisation, and hysteresis loops with well-defined coercive fields.[32] However, both compositions also display conductive behaviour, as evidenced by the tilted, less saturated loop shapes and the observation that maximum polarisation values do not occur at the maximum applied field. And these lossy P-E loops are consistent with the tan δ rising at lower temperatures for decreased ST as shown in Fig. 5. The relatively higher conductivity for lower x compositions is likely attributed to insufficient MnO_2 doping in the BF–ST system, which fails to adequately compensate for charge defects, leading to increased leakage current that affects the loop characteristics. Specifically, for the $x = 0.42$ composition, the P-E loop exhibits a residual polarisation intensity (P_r) of 28 μC cm^{-2} and a coercive field (E_c) of 38 kV cm^{-1}, comparable to reported values of $P_r \sim 30$ μC cm^{-2} and $E_c \sim 40$ kV cm^{-1} in 0.575BF-0.425ST[43] and $P_r \sim 35$ μC cm^{-2} and $E_c \sim 40$ kV cm^{-1} in 0.58BF-0.42ST.[39] The corresponding strain loop shows a maximum strain (S_{max}) of approximately 0.075%. At $x = 0.44$ composition, the P_r decreases to ~24 μC cm^{-2}, while the E_c also decreases to ~33 kV cm^{-1}. The strain response shows an enhancement, with an S_{max} of approximately 0.10%, accompanied by a small negative electrostrictive strain observed in the loop. As the composition increases to $x = 0.46$, the P-E loop becomes noticeably narrower and the S_{max} slightly decreases to 0.097%. These characteristics indicate a transition to typical relaxor ferroelectric behaviour. As shown in Fig. 7, the effect of ST concentration on P_{max}, P_r, and strain (%) is clearly demonstrated. Both P_{max} and P_r exhibit a decreasing trend with increasing ST content. When $x = 0.46$, P_{max} and P_r reach their minimum values of ~28 μC cm^{-2} and ~11 μC cm^{-2}, respectively. Strain shows an increasing trend with increasing ST content, reaching a maximum value of 0.11% at $x = 0.48$.

Combined dielectric data and P-E/S-E loop results reveal that increasing the ST component ratio (x) induces a transition towards a more relaxor-like state in the ceramic. Comparative analysis with our previous research[41] demonstrates that whilst Nb incorporation may reduce T_c and substantially increases E_c in BF–ST systems, the Mn addition investigated in this study exhibits markedly different behaviour. It is worth noting that the grain size (~2 μm) of BF-ST-Nb is comparable to the grain size (1.68–3.90 μm) of BF-ST-Mn in this work. Within this context of similar grain sizes, the BF-ST-Nb composition requires significantly higher applied electric fields to achieve domain switching. For the BF-ST-Mn system, grain size contributed to the E_c values in addition to compositional changes. A clear inverse relationship between average grain size and E_c is evident from Fig. 4 and 6. The sample with the smallest grain size ($x = 0.48$, $D = 1.68$ μm) exhibits the highest E_c (~38 kV cm^{-1}), while the sample with the largest grain size ($x = 0.46$, $D = 3.90$ μm) exhibits the lowest E_c (~21 kV cm^{-1}). This phenomenon can be attributed to the grain boundary pinning effect. Smaller grains increase grain boundary density, where accumulated defects (such as oxygen vacancies) act as pinning

Table 1 T_m of different BF-based ceramics

Composition	T_m (°C)	Frequency (Hz)	References
0.75BF-0.25BT + Mn	619	1 kHz	49
0.73BF-0.25BT-0.02La($Co_{0.5}Mn_{0.5}$)O_3 + Mn	523	1 MHz	50
0.725BF-0.25BT-0.025$Bi_{0.5}K_{0.5}TiO_3$ + Mn	544	1 MHz	51
0.715BF-0.275BT-0.01$Bi_{0.5}Na_{0.5}TiO_3$ + Mn	560	1 MHz	52
0.7BF-0.3BT + Mn	478	100 kHz	53
0.7BF-0.25BT-0.05Bi($Mg_{2/3}Nb_{1/3}$)O_3	450	10 kHz	54
0.7BF-0.25BT-0.05BiScO_3	400	10 kHz	55
0.67BF-0.33BT + Mn	605	1 kHz	49
0.65BF-0.3BT-0.05Bi($Zn_{1/2}Ti_{1/2}$)O_3 + Mn	523	1 MHz	56
0.63BF-0.32BT-0.05Bi($Mg_{2/3}Nb_{1/3}$)O_3	380	10 kHz	54
0.58BF-0.42ST + Mn	382	1 kHz	39
0.575BF-0.425ST + Mn	401	100 kHz	43
0.58BF-0.42ST + Mn	405	100 kHz	This work
0.56BF-0.44ST + Mn	382	100 kHz	This work
0.54BF-0.46ST + Mn	350	100 kHz	This work
0.52BF-0.48ST + Mn	338	100 kHz	This work

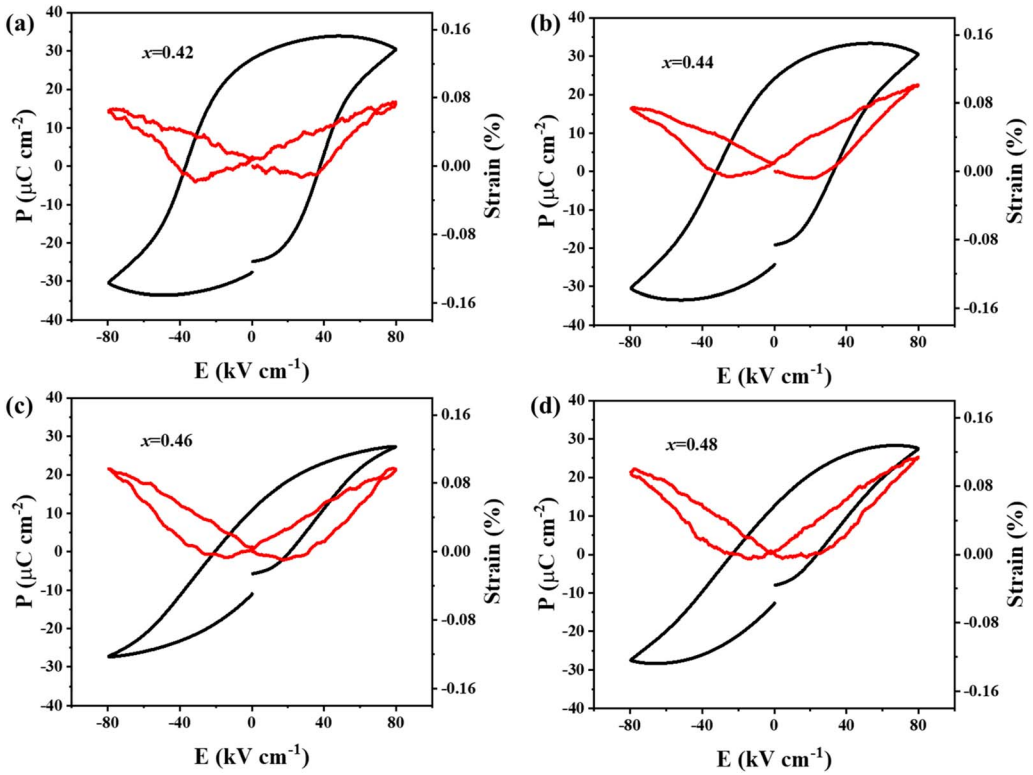

Fig. 6 Room temperature P-E and S-E loops under 80 kV cm^{-1} of (1 − x)BF-xST ceramics, (a) x = 0.42, (b) x = 0.44, (c) x = 0.46, and (d) x = 0.48.

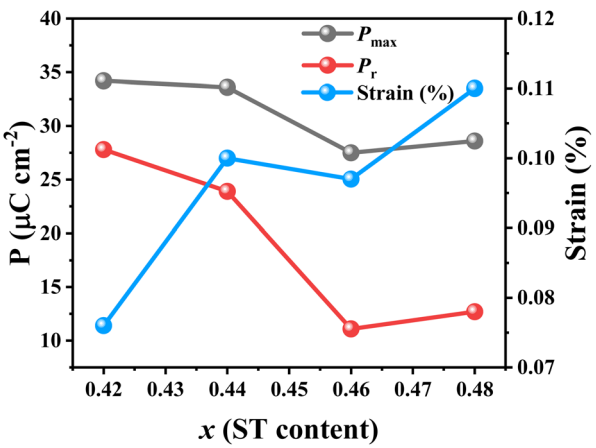

Fig. 7 Effect of ST concentration on P_{max}, P_r, and strain (%).

sites that restrict domain wall movement, thereby requiring a higher E_c for polarisation switching.

Unlike BF–BT, the origin of optimised electrostrain in BF–ST has yet to be elucidated in any report, mainly due to the combination of conductive issues and high E_c. In this study, we attempted to employ *in situ* poling synchrotron XRD to underpin the origin of electrostrain in BF-ST-Mn materials.

3.4 *In situ* poling synchrotron XRD

The optimised ceramic composition, 0.56BF-0.44ST (x = 0.44), was selected for investigation using *in situ* poling synchrotron XRD on unpoled (virgin) ceramic specimens. 3D and contour maps of three representative XRD peaks, $\{200\}_{pc}$, $\{220\}_{pc}$, $\{222\}_{pc}$ at $\psi = 0°$, under application of 2 cycles of AC field (up to ± 80 kV cm^{-1}), were generated by caking the corresponding 2D diffraction rings, Fig. 8a–c. In the virgin sample, three representative peaks were observed as single, corresponding to a pseudo-cubic structure. The XRD peak profiles change position and shape during application of 2 cycles of AC electric field. With increasing electric field at 70 kV cm^{-1}, the $\{222\}_{pc}$ XRD peak is found to split into double, suggesting a structural transformation from pseudo-cubic to rhombohedral. Simultaneously, all three peaks were found to shift to lower 2θ angles (at $\psi = 0°$), corresponding to an increase in the d-spacing and tensile strain. In contrast, all three peaks were found to shift to higher 2θ angles at $\psi = 90°$, Fig. S1, corresponding to a decrease in the d-spacing and compressive strain. In addition, this structural transformation is found to be irreversible, as evidenced by the comparison of the $\{220\}_{pc}$ and $\{222\}_{pc}$ peak profiles between the unpoled and poled states, Fig. 8d. This is different from the previous *in situ* poling synchrotron XRD study on BF-ST-Nb, where a pseudo-cubic structure was obtained before, during and after application of the electric field.[41] This study represents the first synchrotron experiment that demonstrates an irreversible electric field-induced structural transformation from pseudo-cubic to rhombohedral in the BF-ST-Mn solid solution, indicating the non-ergodic relaxor (NR) behaviour of this ceramic composition. Similar NR to long-range ferroelectric (FE) transitions have been reported previously in NBT based ceramics. For example, irreversible

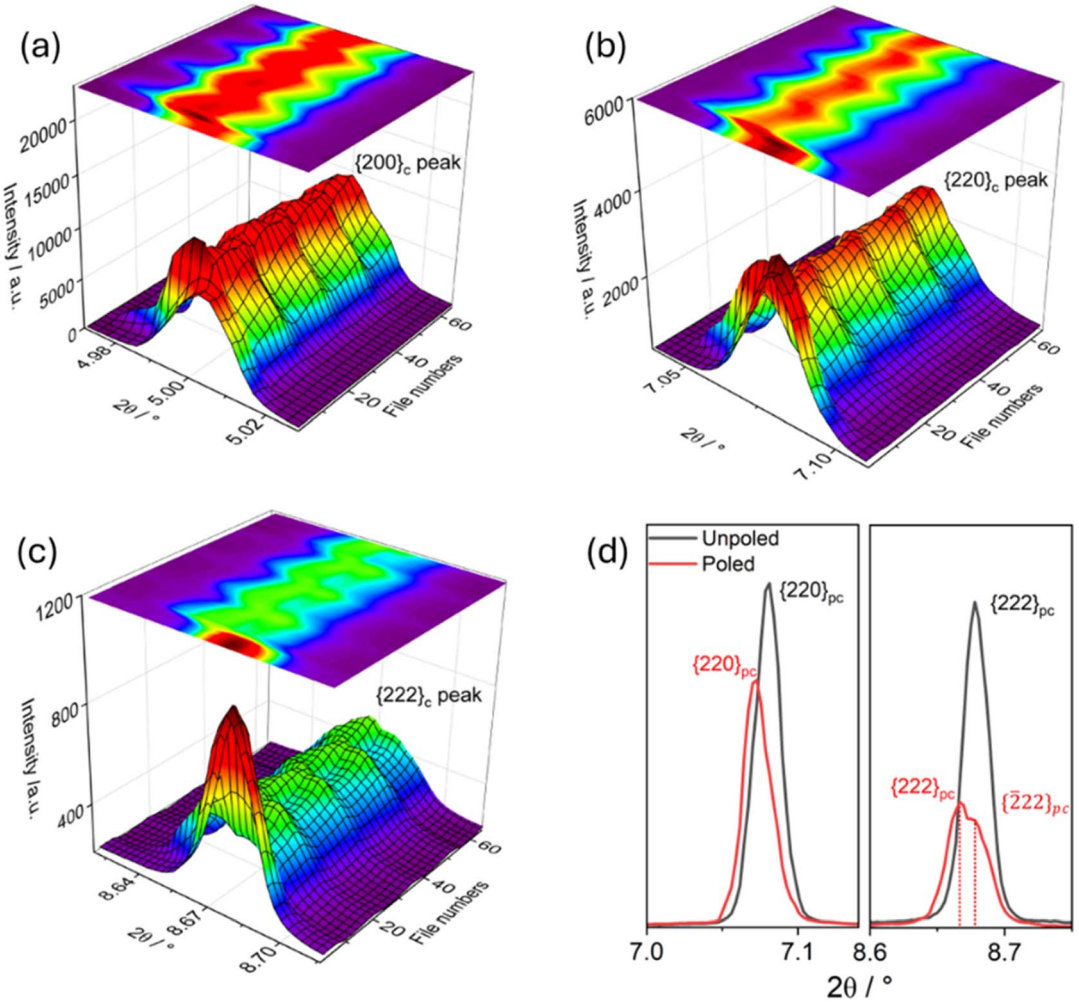

Fig. 8 3D and contour maps of (a) $\{200\}_{pc}$ (b) $\{220\}_{pc}$ and (c) $\{222\}_{pc}$ XRD profiles at $\psi = 0°$ of the $x = 0.44$ ceramic during *in situ* poling synchrotron XRD. (d) Synchrotron XRD profiles at $\psi = 0°$ of unpoled (virgin) and poled specimens of the $x = 0.44$ ceramic.

structural transformations were reported in NBT-0.02$KNbO_3$ (ref. 57) and NBT-0.02$NaNbO_3$ (ref. 37) ceramics, where polarisation, electrostrain and piezoelectric performances were enhanced. However, in BF–BT ceramics, this structural transformation from pseudo-cubic to rhombohedral is almost reversible, leading to an optimised electrostrain of 0.38% at 60 kV cm^{-1} and a large signal piezoelectric coefficient d^*_{33} of 720 pm V^{-1} at 40 kV cm^{-1}.[38]

The estimated electrostrain calculated from three representative peaks during 2 cycles of electric field application was also evaluated, Fig. 9. The synchrotron 1-D XRD peak profiles collected at $\psi = 0°$ and 90° were analyzed, representing directions parallel and perpendicular to the external electric field, respectively. Effective strains (e_{hkl}) of the XRD peaks were calculated based on the weighted d-spacing value (d_{hkl}) using the method described previously.[42] First, all e_{hkl} values at $\psi = 0°$ and 90° were calculated to be positive and negative, respectively, representing elongation (tensile strain) and shrinkage (compressive strain) in directions along and perpendicular to the external electric field. The e_{hkl} *vs.* electric field loop was found to be different during the first cycle and second cycle for both $\psi = 0°$ and 90°. During the first cycle, e_{200}, e_{220} and e_{222} were found to be 0.12%, 0.11%, and 0.14% at $\psi = 0°$, respectively, Fig. 9a, which is approximately twice as much as the absolute value obtained at $y = 90°$ (Fig. 9b). All three e_{hkl} values start from zero and end up with a remanent strain (e_{rem}) after application of one cycle of electric field, corresponding to a phase transition from NR (pseudo-cubic) to FE (rhombohedral). During the second cycle, e_{hkl} starts from the previous value and returns to the same value to form a butterfly-shaped strain loop for both $\psi = 0°$ and 90°, Fig. 9c and d, suggesting the occurrence of domain switching and associated lattice strain. The total effective strain, S_{eff}, calculated using the method described previously,[58] was found to be +0.14% and −0.06% at $\psi = 0°$ and 90°, respectively, during the first cycle of electric field, Fig. 9e. This peak-to-peak S_{eff} was found to be slightly lower during the second cycle of electric field, 0.09% and −0.04% for $\psi = 0°$ and 90°, respectively, Fig. 9f. The S_{eff} matches approximately well with the macroscopic strain obtained from the S-E loop (Fig. 6). Also, the S_{eff} obtained during the first cycle

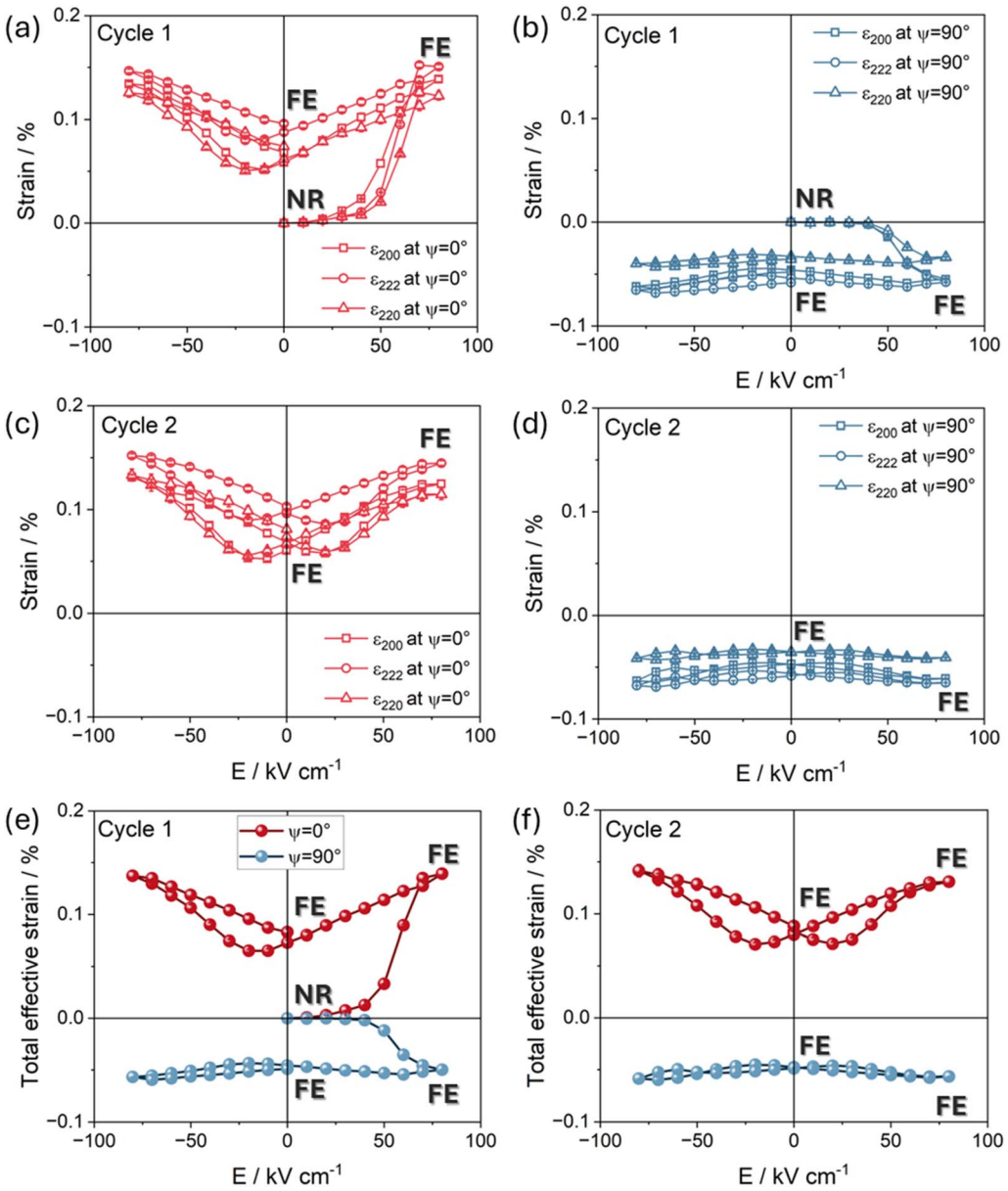

Fig. 9 Effective strain at (a) $\psi = 0°$ and (b) $\psi = 90°$ during the first cycle of electric field. Effective strain at (c) $\psi = 0°$ and (d) $\psi = 90°$ during the second cycle of electric field. Total effective strain during the (e) first cycle and (f) second cycle of electric field.

(0.14%) is higher than that of the second cycle (0.09%), mainly due to the additional contribution from the structural transformation. The electrostrain during the second cycle originates solely from domain switching and the associated lattice strain.

The electrostrain obtained from BF-ST-Mn in this study is higher than that from BF-ST-Nb upon the same electric field. The additional Nb_2O_5 in the previous study aims to minimise electronic conductivity caused by Bi volatilisation and electron hopping between Fe cations.[59] However, E_c (80 kV cm^{-1}) of such ceramic compositions was increased dramatically due to Nb^{5+} donor doping also. Meanwhile, the macroscopic structure was found to remain pseudo-cubic up to 100 kV cm^{-1} without the formation of any long-range ordered ferroelectric structure, indicating an ergodic relaxor behaviour.[41] The origin of electrostrain in 0.6BF-0.4ST-Nb ceramics thus was found to be dominated by lattice-to-lattice and/or short-range local distortions. In contrast to previous studies, the origin of electrostrain in 0.56BF-0.44ST-Mn ceramics was found to result from a combination of a structural transformation from pseudo-cubic (NR) to rhombohedral (FE), followed by FE domain switching, resulting in superior ferroelectric and electrostrain performance compared to BF-ST-Nb ceramics.

The ferroelectric switching behaviour exhibits a striking divergence between Nb and Mn additions, with Nb-containing ceramics displaying significantly elevated E_c. To rationalise this contrast, we propose a defect chemistry framework rooted in established principles: (1) air-sintered BF-based materials exhibit p-type conductivity arising from volatilisation of Bi or/and Fe^{3+} oxidation to Fe^{4+} due to oxygen uptake during cooling from the sintering temperature,[60–62] as shown in eqn (1)–(1″)

and (2) Both Mn and Nb substitute onto the Fe site to compensate valence fluctuations, as Ti^{4+} reduction is kinetically unfavourable at moderate sintering temperatures (~1100–1150 °C). Whilst both dopants effectively suppress p-type hole conduction, they do so through fundamentally different mechanisms.

In $BiFeO_3$-based ceramics, volatilisation at sintering temperature is likely to create defects as shown in eqn (1). On cooling, reoxidation may occur according to eqn (1′). The origin of p-type conduction can be expressed in a simplified form as eqn (1″), where the generation of holes ($h^{\bullet}$) is explicitly shown.

$$2Bi_{Bi}^{\times} + 3O_O^{\times} \leftrightarrow 2V_{Bi}^{'''} + 3V_O^{\bullet\bullet} + Bi_2O_3(g) \quad (1)$$

$$2Fe_{Fe}^{\times} + V_O^{\bullet\bullet} + \frac{1}{2}O_2(g) \leftrightarrow 2Fe_{Fe}^{\bullet} + O_O^{\times} \quad (1')$$

$$V_O^{\bullet\bullet} + \frac{1}{2}O_2(g) \leftrightarrow O_O^{\times} + 2h^{\bullet} \quad (1'')$$

Now let's consider the presence of aliovalent dopants, which can act as acceptors or donors, when substituting for Fe^{3+}. The following cases can occur. If a donor is incorporated, its charge can be compensated either electronically (suppressing conduction) or by cation vacancies.[63] For example, Nb^{5+} replacing Fe^{3+} can be compensated by A-site vacancies ($V_{Bi}^{'''}$) in $BiFeO_3$-based ceramics, as follows,

$$Bi_2O_3 + 3Nb_2O_5 \leftrightarrow 2Bi_{Bi}^{\times} + 4V_{Bi}^{'''} + 6Nb_{Fe}^{\bullet\bullet} + 18O_O^{\times} \quad (2)$$

Given that MnO_2 was used as the additive in this work, we anticipate a dynamic multivalency equilibrium predominantly involving Mn^{3+} and Mn^{2+} oxidation states in the matrix at high sintering temperatures.[64] Whilst Mn^{3+} typically forms a neutral defect requiring no direct charge compensation. it can also act as an electron donor through redox equilibrium with host iron ($Mn^{3+} + Fe^{4+} \leftrightarrow Mn^{4+} + Fe^{3+}$), effectively reducing Fe^{4+}-associated mobile holes. With Mn addition, the dominant Mn^{3+} species (high-spin state, ~0.645 Å) exhibits near-perfect ionic radius matching with the host Fe^{3+} (~0.645 Å), producing negligible lattice strain. Mn^{4+} creates singly-charged positive defects ($Mn_{Fe}^{\bullet}$) that annihilate p-type holes. And eqn (3) also illustrates the parallel ionic compensation mechanism for this donor defect, which is achieved by the formation of $V_{Bi}^{'''}$:

$$Bi_2O_3 + 3MnO_2 \leftrightarrow 2Bi_{Bi}^{\times} + V_{Bi}^{'''} + 3Mn_{Fe}^{\bullet} + 9O_O^{\times} \quad (3)$$

Although minority Mn^{4+} species (~0.530 Å) introduce local elastic distortion, the overall pinning landscape remains moderate. This moderate pinning is primarily characterised by Mn^{2+} induced defect dipoles ($Mn_{Fe}^{'} - V_O^{\bullet\bullet}$), as shown in eqn (4).

$$Bi_2O_3 + 2MnO \leftrightarrow 2Bi_{Bi}^{\times} + 2Mn_{Fe}^{'} + V_O^{\bullet\bullet} + 5O_O^{\times} \quad (4)$$

This localised chemical and strain disorder that stabilises a non-ergodic relaxor state with pseudo-cubic symmetry. Critically, the moderate pinning strength proves insufficient under high applied fields, which successfully overcome the existing potential barriers (including $Mn_{Fe}^{'} - V_O^{\bullet\bullet}$ defect dipoles), nucleating stable domain walls and driving an irreversible transition to a long-range ordered rhombohedral ferroelectric phase. Notably, the 0.2 wt% MnO_2 employed here (~0.6 mol%) represents lower doping than the 1 mol% Nb_2O_5 used in our previous work.[41]

Despite comparable ionic radius matching (~0.640 Å with Fe^{3+}), the $Nb_{Fe}^{\bullet\bullet}$ defect fundamentally alters the pinning mechanism: its +2 relative charge (double that of Mn^{4+}) creates deep electrostatic potential wells that dominate the defect chemistry. These strong positive centres couple intensely with negatively charged background defects (*e.g.*, $V_{Bi}^{'''}$), generated during charge compensation (as shown in eqn (2)), forming stable dipolar complexes that rigidly anchor domain walls through electrostatic clamping. The energy barrier for domain wall depinning thus scales with the +2 electrostatic potential, substantially exceeding the mixed elastic/weak-electrostatic barrier with Mn addition and directly explaining the elevated E_c. More profoundly, the powerful coulombic forces from $Nb_{Fe}^{\bullet\bullet}$ generate intense random fields throughout the lattice. Whilst Nb^{5+} (d^0 configuration) is ferroelectrically active and promotes local polar ordering, the strong random fields simultaneously frustrate long-range coupling of polar nanoregions (PNRs). These random fields perpetually pin and confine PNRs, preventing their coalescence into macroscopic domains even under fields up to 100 kV cm^{-1}, thereby maintaining the ergodic relaxor character with average pseudo-cubic structure.

4. Conclusion

In summary, the systematic investigation of dielectric properties revealed critical insights into the relaxor-to-ferroelectric transition, with increasing ST content progressively broadening dielectric peaks and reducing frequency dispersion effects. The observed decrease in ε_m and T_m with increasing x demonstrates the profound influence of chemical composition on polar ordering. These dielectric characteristics directly correlate with the enhanced relaxor behaviour that enables the observed electrostrain mechanisms. Ferroelectric characterisation established the evolution from conventional ferroelectric loops ($x = 0.42$, 0.44) to relaxor behaviour ($x = 0.46$, 0.48), with corresponding changes in E_c and P_r. The progression from typical hysteretic P-E loops to constricted characteristics reflects the underlying structural disorder that facilitates the irreversible phase transitions.

The *in situ* poling synchrotron XRD provides critical insights into the electrostrain mechanisms. The observed irreversible phase transition from non-ergodic relaxor to long-range ferroelectric behavior is analogous to that reported in NBT-based systems but represents the first such demonstration in BF–ST solid solutions. This finding establishes a new paradigm for optimising electrostrain in BF-based ceramics and suggests that careful addition selection can fundamentally alter the field-response mechanisms. Future investigations may explore compositional fine-tuning around the optimal $x = 0.44$ region.

Conflicts of interest

The authors declare that they have no known competing financial interests or personal relationships that could have appeared to influence the work reported in this paper.

Data availability

The data supporting this article have been included as part of the supplementary information (SI). Supplementary information: summary of XRD Rietveld refinement results and additional *in situ* poling synchrotron XRD data. See DOI: https://doi.org/10.1039/d5ta07591b.

Acknowledgements

The authors gratefully acknowledge the support of the Dame Kathleen Ollerenshaw Fellowship and Dean's PhD Scholarship provided by The University of Manchester, and the Royal Society of Chemistry Research Fund Grant R23-0577995877 and R23-5982928392. We also thank Diamond Light Source for access to beamline I15 (proposal number CY36011-1) that contributed to the results presented here. Additionally, we thank David A. Hall (The University of Manchester) for assistance with sample testing.

References

1 W. Zhuang, *et al.*, Enhanced piezoelectric properties in low-temperature sintered Pb(Zr,Ti)O_3-based ceramics via Yb_2O_3 doping, *J. Adv. Dielectr.*, 2024, **14**(04), 2340008.
2 Z. Ma, *et al.*, Optimization of energy storage properties in (1 −x)$Na_{0.5}Bi_{0.5}TiO_3$-x$Sr_{0.7}La_{0.2}TiO_3$-relaxed ferroelectric ceramics, *J. Adv. Dielectr.*, 2022, **13**(01), 2242003.
3 C. Wang and X. J. Lou, High energy storage properties of 0.94$Bi_{0.5}Na_{0.5}TiO_3$-0.06$BaTiO_3$ ceramics by incorporating $Sr_{0.8}Bi_{0.1}\gamma_{0.1}Ti_{0.8}Zr_{0.2}O_{2.95}$, *Microstructures*, 2023, 1–2.
4 L. Yang, *et al.*, Perovskite lead-free dielectrics for energy storage applications, *Prog. Mater. Sci.*, 2019, **102**, 72–108.
5 H. Zubairi, *et al.*, Current development, optimisation strategies and future perspectives for lead-free dielectric ceramics in high field and high energy density capacitors, *Chem. Soc. Rev.*, 2024, **53**(21), 10761–10790.
6 S.-E. Park and T. R. Shrout, Ultrahigh strain and piezoelectric behavior in relaxor based ferroelectric single crystals, *J. Appl. Phys.*, 1997, **82**(4), 1804–1811.
7 M. Ahart, *et al.*, Origin of morphotropic phase boundaries in ferroelectrics, *Nature*, 2008, **451**(7178), 545–548.
8 J. Rödel, *et al.*, Perspective on the Development of Lead-free Piezoceramics, *J. Am. Ceram. Soc.*, 2009, **92**(6), 1153–1177.
9 E. Aksel and J. L. Jones, Advances in lead-free piezoelectric materials for sensors and actuators, *Sensors*, 2010, **10**(3), 1935–1954.
10 J. Wu, Perovskite lead-free piezoelectric ceramics, *J. Appl. Phys.*, 2020, **127**(19), 190901.
11 T. R. Shrout and S. J. Zhang, Lead-free piezoelectric ceramics: Alternatives for PZT?, *J. Electroceram.*, 2007, **19**(1), 113–126.
12 J. F. Li, *et al.*, (K,Na)NbO_3-Based Lead-Free Piezoceramics: Fundamental Aspects, Processing Technologies, and Remaining Challenges, *J. Am. Ceram. Soc.*, 2013, **96**(12), 3677–3696.
13 A. R. Paterson, *et al.*, Relaxor-ferroelectric transitions: Sodium bismuth titanate derivatives, *MRS Bull.*, 2018, **43**(8), 600–606.
14 T. Takenaka, K.-i. Maruyama and K. Sakata, ($Bi_{1/2}Na_{1/2}$)TiO_3-$BaTiO_3$ System for Lead-Free Piezoelectric Ceramics, *Jpn. J. Appl. Phys.*, 1991, **30**, 2236–2239.
15 D. Wang, *et al.*, $BiFeO_3$-$BaTiO_3$: A new generation of lead-free electroceramics, *J. Adv. Dielectr.*, 2019, **08**(06), 1830004.
16 Y. Wang, *et al.*, Compositional Inhomogeneity in Li- and Ta-Modified (K, Na)NbO_3 Ceramics, *J. Am. Ceram. Soc.*, 2007, **90**(11), 3485–3489.
17 T. Rowe, J. S. Forrester and J. L. Jones, On the synthesis of potassium sodium niobate, II: the use of $KNaCO_3$ to synthesize more compositionally homogeneous materials and at lower temperatures, *J. Mater. Sci.*, 2025, 11801–11813.
18 X. Liu and X. Tan, Giant Strains in Non-Textured ($Bi_{1/2}$ $Na_{1/2}$) TiO_3 -Based Lead-Free Ceramics, *Adv. Mater.*, 2016, **28**(3), 574–578.
19 J. Yin, *et al.*, Superior and anti-fatigue electro-strain in $Bi_{0.5}Na_{0.5}TiO_3$-based polycrystalline relaxor ferroelectrics, *J. Mater. Chem. A*, 2019, 7(10), 5391–5401.
20 T. Zheng, *et al.*, Recent development in lead-free perovskite piezoelectric bulk materials, *Prog. Mater. Sci.*, 2018, **98**, 552–624.
21 J. Wang, J. B. Neaton, H. Zheng, V. Nagarajan, S. B. Ogale, B. Liu, D. Viehland, V. Vaithyanathan, D. G. Schlom, U. V. Waghmare, N. A. Spaldin, K. M. Rabe, M. Wuttig and R. Ramesh, Epitaxial $BiFeO_3$ Multiferroic Thin Film Heterostructures, *Science*, 2003, **299**(5613), 1719–1722.
22 G. Gupta, *et al.*, Visible-light driven excellent photocatalytic degradation of ofloxacin antibiotic using $BiFeO_3$ nanoparticles, *Chemosphere*, 2023, **314**, 137611.
23 A. Iacomini, *et al.*, Tuning the electrical conductivity and Maxwell-Wagner relaxation in $BiFeO_3$–$BaTiO_3$ piezoceramics, *J. Eur. Ceram. Soc.*, 2024, **44**(12), 6948–6959.
24 B. Li, *et al.*, Optimizing electro-strain via manipulating the oxygen octahedral structure in BF-BT-based ceramics, *Phys. Chem. Chem. Phys.*, 2022, **24**(48), 29891–29901.
25 B. Li, T. Zheng and J. Wu, Structural disorder and oxygen octahedron evolution via defect engineering for properties enhancement in BF–BT ceramics, *J. Am. Ceram. Soc.*, 2024, **107**(7), 4789–4800.
26 T. Zheng, Y. Ding and J. Wu, Bi nonstoichiometry and composition engineering in (1 −x)$Bi_{1+y}FeO_{3+3y/2}$ − x$BaTiO_3$ ceramics, *RSC Adv.*, 2016, **6**(93), 9831–9839.
27 Y. Wei, *et al.*, Dielectric, ferroelectric, and piezoelectric properties of $BiFeO_3$–$BaTiO_3$ ceramics, *J. Am. Ceram. Soc.*, 2013, **96**(10), 3163–3168.
28 L. Wang, *et al.*, Effect of PMN content on the phase structure and electrical properties of PMN–PZT ceramics, *Ceram. Int.*, 2013, **39**(7), 8571–8574.
29 X. Gao, *et al.*, Giant Piezoelectric Coefficients in Relaxor Piezoelectric Ceramic PNN-PZT for Vibration Energy Harvesting, *Adv. Funct. Mater.*, 2018, **28**(30), 1–8.

30 L. Sun, *et al.*, Enhanced piezoelectric response and Curie temperature of $BiFeO_3$-$BaTiO_3$ by substituting $PbTiO_3$ for $BaTiO_3$, *Ceram. Int.*, 2025, 24945–24951.
31 M. Habib, *et al.*, High and temperature-insensitive piezoelectric performance in the lead-free Sm-doped $BiFeO_3$–$BaTiO_3$ ceramics with high Curie temperature, *Ceram. Int.*, 2022, **48**(18), 26608–26617.
32 D. Damjanovic, Ferroelectric, dielectric and piezoelectric properties of ferroelectric thin films and ceramics, *Rep. Prog. Phys.*, 1998, **61**(9), 1267–1324.
33 F. Luo, *et al.*, Achieving large strain and low hysteresis in $BiFeO_3$-$BaTiO_3$-based piezoelectric ceramics, *Ceram. Int.*, 2024, **50**(16), 27846–27855.
34 J. Hao, *et al.*, Progress in high-strain perovskite piezoelectric ceramics, *Mater. Sci. Eng., R*, 2019, **135**, 1–57.
35 A. Pramanick, *et al.*, Origins of Electro-Mechanical Coupling in Polycrystalline Ferroelectrics During Subcoercive Electrical Loading, *J. Am. Ceram. Soc.*, 2011, **94**(2), 293–309.
36 X. Liu, *et al.*, Composition-induced structural transitions and enhanced strain response in nonstoichiometric NBT-based ceramics, *J. Am. Ceram. Soc.*, 2017, **100**(8), 3636–3645.
37 G. Wang, *et al.*, Electric field-induced irreversible relaxor to ferroelectric phase transformations in $Na_{0.5}Bi_{0.}5TiO_3$-$NaNbO_3$ ceramics, *J. Am. Ceram. Soc.*, 2019, **102**(12), 7746–7754.
38 J. Chen, *et al.*, Origin of large electric-field-induced strain in pseudo-cubic $BiFeO_3$–$BaTiO_3$ ceramics, *Acta Mater.*, 2020, **197**, 1–9.
39 S. Wang, *et al.*, Microstructure, dielectric, and piezoelectric properties of $BiFeO_3$–$SrTiO_3$ lead-free ceramics, *J. Am. Ceram. Soc.*, 2023, **107**(1), 205–213.
40 Y. Wang, *et al.*, Microstructure and electrical properties of Nb-doped $SrTiO_3$-$BiFeO_3$ based lead-free ceramics, *J. Am. Ceram. Soc.*, 2021, **105**(3), 2020–2028.
41 Z. Lu, *et al.*, In situ poling X-ray diffraction studies of lead-free $BiFeO_3$–$SrTiO_3$ ceramics, *Mater. Today Phys.*, 2021, **19**, 1–8.
42 G. Wang, *et al.*, Origin of the large electrostrain in $BiFeO_3$-$BaTiO_3$ based lead-free ceramics, *J. Mater. Chem. A*, 2019, **7**(37), 21254–21263.
43 M. Makarovic, *et al.*, Processing, piezoelectric and ferroelectric properties of (x)$BiFeO_3$-(1-x)$SrTiO_3$ ceramics, *J. Eur. Ceram. Soc.*, 2019, **39**(13), 3693–3702.
44 N. Horchidan, *et al.*, A comparative study of hard/soft PZT-based ceramic composites, *Ceram. Int.*, 2016, **42**(7), 9125–9132.
45 Y. H. Huang, *et al.*, Defect dipoles induced high-energy storage density in Mn-doped BST ceramics prepared by spark plasma sintering, *J. Am. Ceram. Soc.*, 2018, **102**(4), 1904–1911.
46 M. Liu, *et al.*, Fine-grained silica-coated barium strontium titanate ceramics with high energy storage, *Ceram. Int.*, 2018, **44**(16), 20239–20244.
47 A. A. Bokovm and Z.-G. Ye, Recent progress in relaxor ferroelectrics with perovskite structure, *J. Mater. Sci.*, 2006, **41**(1), 31–52.
48 W. Liu and X. Ren, Large piezoelectric effect in Pb-free ceramics, *Phys. Rev. Lett.*, 2009, **103**(25), 257602.
49 S. O. Leontsev and R. E. Eitel, Dielectric and Piezoelectric Properties in Mn-Modified (1−x)$BiFeO_3$–x$BaTiO_3$ Ceramics, *J. Am. Ceram. Soc.*, 2009, **92**(12), 2957–2961.
50 L. Luo, *et al.*, Phase transition, piezoelectric, and multiferroic properties of $La(Co_{0.5}Mn_{0.5})O_3$-modified $BiFeO_3$-$BaTiO_3$ lead-free ceramics, *Phys. Status Solidi A*, 2015, **212**(9), 2012–2022.
51 D. Lin, *et al.*, Microstructure, ferroelectric and piezoelectric properties of $Bi_{0.5}K_{0.5}TiO_3$-modified $BiFeO_3$–$BaTiO_3$ lead-free ceramics with high Curie temperature, *J. Eur. Ceram. Soc.*, 2013, **33**(15–16), 3023–3036.
52 Y. Li, *et al.*, Structure, Ferroelectric, Piezoelectric, and Ferromagnetic Properties of $BiFeO_3$-$BaTiO_3$-$Bi_{0.5}Na_{0.5}TiO_3$ Lead-Free Multiferroic Ceramics, *J. Am. Ceram. Soc.*, 2014, **97**(11), 3602–3608.
53 D. Wang, *et al.*, Temperature dependent, large electromechanical strain in Nd-doped $BiFeO_3$-$BaTiO_3$ lead-free ceramics, *J. Eur. Ceram. Soc.*, 2017, **37**(4), 1857–1860.
54 S. Murakami, *et al.*, High strain (0.4%) $Bi(Mg_{2/3}Nb_{1/3})O_3$-$BaTiO_3$-$BiFeO_3$ lead-free piezoelectric ceramics and multilayers, *J. Am. Ceram. Soc.*, 2018, **101**(12), 5428–5442.
55 S. Murakami, *et al.*, Optimising dopants and properties in $BiMeO_3$ (Me = Al, Ga, Sc, Y, $Mg_{2/3}Nb_{1/3}$, $Zn_{2/3}Nb_{1/3}$, $Zn_{1/2}Ti_{1/2}$) lead-free $BaTiO_3$-$BiFeO_3$ based ceramics for actuator applications, *J. Eur. Ceram. Soc.*, 2018, **38**(12), 4220–4231.
56 Q. Zheng, *et al.*, Microstructure, ferroelectric, piezoelectric and ferromagnetic properties of $BiFeO_3$–$BaTiO_3$–$Bi(Zn_{0.5}Ti_{0.5})O_3$ lead-free multiferroic ceramics, *J. Mater. Sci.: Mater. Electron.*, 2014, **25**(6), 2638–2648.
57 G. Wang, *et al.*, Structural characterization of the electric field-induced ferroelectric phase in $Na_{0.5}Bi_{0.5}TiO_3$-$KNbO_3$ ceramics, *J. Eur. Ceram. Soc.*, 2016, **36**(16), 4015–4021.
58 M. R. Daymond, The determination of a continuum mechanics equivalent elastic strain from the analysis of multiple diffraction peaks, *J. Appl. Phys.*, 2004, **96**(8), 4263–4272.
59 Z. Lu, *et al.*, Superior energy density through tailored dopant strategies in multilayer ceramic capacitors, *Energy Environ. Sci.*, 2020, **13**(9), 2938–2948.
60 E. T. Wefring, *et al.*, Electrical conductivity and ferroelastic properties of Ti-substituted solid solutions (1−x) $BiFeO_{3-x}Bi_{0.\ 5}K_{0.\ 5}TiO_3$, *J. Eur. Ceram. Soc.*, 2016, **36**(3), 497–506.
61 M. Makarovic, *et al.*, Tailoring the electrical conductivity and hardening in $BiFeO_3$ ceramics, *J. Eur. Ceram. Soc.*, 2020, **40**(15), 5483–5493.
62 T. Rojac, *et al.*, Domain-wall conduction in ferroelectric $BiFeO_3$ controlled by accumulation of charged defects, *Nat. Mater.*, 2017, **16**(3), 322–327.
63 S. Presto, *et al.*, Application of La-doped $SrTiO_3$ in advanced metal-supported solid oxide fuel cells, *Crystals*, 2018, **8**(3), 134.
64 F. Zeng, C. Zhou, W. cai, G. Zhang, H. Zhang and G. Fan, *Mater. Res. Bull.*, 2022, **147**, 111617.